



Modulation of electronic density in ultrathin g-C₃N₄ for enhanced photocatalytic hydrogen evolution through an efficient hydrogen spillover pathway

Fangfang Gao¹, Han Xiao¹, Jiarui Yang, Xue Luan, Duoduo Fang, Lei Yang, Jiangzhi Zi, Zichao Lian*

School of Materials and Chemistry, University of Shanghai for Science and Technology, Shanghai 200093, P. R. China



ARTICLE INFO

Keywords:

Carbon nitride
B
P-doped g-C₃N₄
Hydrogen spillover
photoinduced carrier dynamics
Photocatalytic hydrogen evolution

ABSTRACT

The high recombination of photoinduced electron-hole and deep charge trapping in graphitic carbon nitride (g-C₃N₄)-based photocatalysts have limited the photocatalytic activity in hydrogen evolution reaction (HER). Here, we proposed the synergistic strategies of electron-deficient boron (B) and electron-rich phosphorus (P) doped g-C₃N₄ (BPCN) through tuning the electron density for enhanced photocatalytic activity in HER under visible light irradiation. The BPCN exhibited highest photocatalytic activity in HER with the apparent quantum efficiency of 17.4% at 400 nm superior to reported g-C₃N₄-based photocatalysts. The remarkable activity in HER was attributed to the efficient charge separation by the shallow charge capture, electron transfer from P to B and the efficient hydrogen spillover pathway occurred by the strong absorption H₂O at P sites and then H transferring to B sites. This work paves a new route to changing the electronic density with the tunable band structures through the doping engineering for enhanced photocatalytic activity.

1. Introduction

The wide application of photocatalysis technology in environmental remediation, energy production and photochemical synthesis attracted much attention due to environmentally friendly, clean and zero-pollution [1–6]. Many efforts have been devoted to using semiconductor photocatalysts for water splitting to hydrogen to alleviate modern energy crisis [7–10]. Among them, the metal-free polymer graphite carbon nitride (g-C₃N₄) as a typical visible light-driven photocatalyst, has attracted great interests due to its suitable band structure for hydrogen evolution reaction (HER), high thermal and chemical stability, and low cost [11–13]. However, the heavily limitation of the pure g-C₃N₄ was the rapid photoinduced carrier recombination, deep trapping sites, low surface area, and low active site density [14–18]. One effective strategy is elevating the shallow charge trapping sites in the band structure of g-C₃N₄ by suppressing the intrinsic deep-charge trapping sites for accelerating the active electrons transport.

Compared with the constructions of heterojunction photocatalysts to improving the photocatalytic activity, the elemental doping

heteroatoms in g-C₃N₄ could easily tune the electrical and optical properties of g-C₃N₄ at the atomic levels [19–21]. Specifically, the non-metal heteroatomic dopants such as nitrogen (N) [22], oxygen O [23], sulfur (S) [24], phosphorus (P) [25] and boron (B) [26] play a crucial role in promoting the photocatalytic activity of g-C₃N₄, which has a wider light response range, smaller band gap and higher light utilization efficiency, such as adjusting the band structures, narrowing the optical band gap and improving charge transport. However, the roles of each element in g-C₃N₄ affecting the relationships between the pathway of the photogenerated carrier transfer and the photocatalytic activity in HER processes have been rarely investigated.

Here, we successfully synthesized the ultrathin of g-C₃N₄ with electron deficient B and electron rich P co-doping (BPCN) via a simple thermal treatment strategy as a typical model to investigate the relationships between the tune of the electronic density and photocatalytic HER. The BPCN could be easily tuned the band structure and charge carrier migration by the doping methods. The BPCN exhibited higher photocatalytic activity in HER (4579 $\mu\text{mol h}^{-1} \text{g}^{-1}$) than that of B-doped g-C₃N₄ (BCN, 2310 $\mu\text{mol h}^{-1} \text{g}^{-1}$), P-doped g-C₃N₄ (PCN, 1346 $\mu\text{mol h}^{-1} \text{g}^{-1}$)

* Corresponding author.

E-mail address: zichaolian@usst.edu.cn (Z. Lian).

¹ Fangfang Gao and Han Xiao equally contributed to this work.

g^{-1}), bulk g-C₃N₄ (CN, 154 $\mu\text{mol h}^{-1} \text{g}^{-1}$) and ultrathin g-C₃N₄ (ECN, 538 $\mu\text{mol h}^{-1} \text{g}^{-1}$) under visible light irradiation. The remarkable performance and excellent stability were attributed to the efficient charge separation by the shallow trapping of the hot electrons and the increase of the conduction band potentials to boost both the kinetic and thermodynamic driving forces for photocatalytic H₂ production. Density functional theory (DFT) calculation revealed that the electron from the electron-rich P replacing bridge site C could be transferred to the electron-deficient B replacing the edge N position of heptazine unit, and the hydrogen spillover could improve the strong absorption of OH* on the P sites and then the H* on B sites for enhanced photocatalytic activity in HER. The design of the codoping photocatalysts could provide an effective way for constructing the photocatalytic hydrogen system with high efficiency and stability.

2. Experimental section

2.1. Material

2.1.1. Synthesis of Bulk CN and PCN

The mixture of the melamine (5 g) and diammonium hydrogen phosphate ((NH₄)₂HPO₄, 0.5 g) was added into the mortar and thoroughly ground and mixed, then put into the covered crucible. It was heated to 550 °C in Muffle furnace at 5 °C min⁻¹, and kept at this temperature for 2 h. The resultant product was finely grounded into powder, washed twice with deionized water to remove the incomplete (NH₄)₂HPO₄. Finally, it was dried overnight in vacuum at 60 °C. The as-obtained sample was named as the PCN. The X in PCNX (PCN0.1, PCN0.3 and PCN0.5) referred to the amount of the added (NH₄)₂HPO₄ as 0.1 g, 0.3 g, and 0.5 g, respectively. The synthetic processes of the bulk g-C₃N₄ (CN) were the same procedures without adding the phosphorus source.

2.1.2. Synthesis of the BCN and BPCN

The synthetic procedures of the BPCN were following. Briefly, the mixture of the PCN (0.40 g) and NaBH₄ (0.27 g) was grounded in a mortar. It was heated to 400 °C at the rate of 7 °C min⁻¹ in a tubular furnace under a N₂ atmosphere and kept for 1 h. The as-obtained sample was washed twice with deionized water, then placed in a certain amount of ethanol solution by the ultrasonication for 1 h. Finally, it was freeze-dried for 12 h to get the BPCN. The Y in the BPCNY (BPCN0.5 BPCN1, BPCN1.5 (in paper), BPCN2) referred to the weight ratio between the PCN and NaBH₄ in the synthesized procedures. The preparation procedures of the BCN were similar to the above method using the mixture of the bulk CN (0.4 g) and NaBH₄ (0.16 g).

2.2. Characterization

Transmission electron microscopy (TEM) was performed on a HT7800 (Hitachi) operating an acceleration voltage of 120 kV. Atomic force microscope (AFM) measurement was performed on a Dimension Icon. X-ray diffraction (XRD) measurements were measured using a D/MAX-2000 with Cu K α radiation ($\lambda = 1.5406 \text{ \AA}$) at 40 kV and 30 mA. Fourier Transform Infrared (FTIR) measurements was carried out on Bruker Vertex 80 V. The UV-vis diffuse reflectance spectra (UV-vis DRS) measurements of all samples were performed using a UH5700 (Hitachi) spectrophotometer. The BET surface area and pore diameter distribution of the photocatalysts were done by using Micromeritics ASAP2460 (Micromeritics Instrument Corp). X-ray photoelectron spectroscopy (XPS) measurements was carried out on thermo fisher Scientific K-Alpha+ spectrometer with a 300 W Al K α radiation source. Carbon (C 1 s = 284.8 eV) was served as a reference for calibrating the binding energies. The room temperature PL spectra were recorded with an excitation wavelength of 375 nm. Time-resolved fluorescence decay spectra were acquired with an EI FLS-1000 fluorescence spectrometer.

2.3. Photocatalytic hydrogen evolution

Briefly, 5.0 mg photocatalyst and a certain amount of H₂PtCl₆·6 H₂O (1.0 wt% Pt) were mixed and suspended into a 10 vol% triethanolamine aqueous solution under magnetic stirring and sonication in a 3 mL sealed Pyrex flask. Before photocatalytic tests, the above-mentioned suspension was purged via 30 min Argon bubbling to remove oxygen species (e.g., dissolved oxygen). The samples were then irradiated with a 300-W Xe lamp (MAX-303A, Beijing newbit Technology Co., Ltd) through an ultraviolet-visible cutoff filter ($> 420 \text{ nm}$), which was 5 cm away from the reactor as a visible light source and light density was 100 mW cm⁻², for various reaction times. The hydrogen evolution was measured with a gas chromatograph (GC-2014, Shimadzu, with nitrogen as a carrier gas) by using a thermal conductivity detector.

Apparent quantum yields (AQYs) were measured at various single wavelengths, via band-pass filters, under the same HER conditions using the following Eq. (1). The focused intensity of the light source at the liquid level was measured with a photo-radiometer (CEL-NP2000-2).

$$\text{AQY} = \frac{\text{number of reacted electrons}}{\text{number of incident photons}} \times 100\% \\ = \frac{\text{number of evolved H}_2 \text{ molecules} \times 2}{\text{number of incident photons}} \times 100\% \quad (1)$$

2.4. Photoelectrochemical (PEC) measurements

The PEC measurements were conducted in a conventional three-electrode system using a single-compartment quartz cell on an electrochemical station (CHI-660E). The 0.5 M Na₂SO₄ aqueous solution (pH = 6.8) was used as the electrolyte for PEC measurements. A 150 μL solution was used from the mixture of Nafion solution (10 μL , 5%), the photocatalyst (3 mg), and ethanol (500 μL) and slowly dropped onto FTO conductive glass ($A = 1 \text{ cm}^2$). Then it was dried in the vacuum at 60 °C for 1 h to prepare the working electrodes. A silver chloride electrode (Ag/AgCl) and Pt sheet electrode were used as reference and counter electrodes, respectively. Both the photocurrent and AC impedance measurements were performed at 0.8 V bias voltage and illumination ($\lambda > 420 \text{ nm}$). A 300 W Xe lamp with an ultraviolet (UV) filter ($\lambda > 420 \text{ nm}$) was placed 5 cm away from the photoelectrochemical cell as a visible light source. The open-circuit voltage of the impedance test is in the frequency range of $10^5 \sim 10^{-2} \text{ Hz}$ with an AC voltage at 5 mV s⁻¹.

2.5. Transient absorption (TA) measurements

The fs-TAS measurements were collected with a femtosecond Ti/Sapphire regenerative amplifier laser system (Spitfire-Pro, Spectra-Physics Company), and an automated data acquisition transient absorption spectrometer (Ultrafast, Helios) was used to record the transient absorption spectra of the photocatalysts. The amplifier was seeded with the laser output from the oscillator (Vitara, Coherent Inc.) and generated about 35 fs pulse at 800 nm with a repetition rate of 1 kHz and an average power is around 7.0 W. In our experiments, part of these fundamental pulse (2.0 W of the amplified 800 nm output from the Astrella) were used to second harmonic generator BBO crystal to obtain the laser of 400 nm as pump, and the probe pulse was obtained by using the amplified 800 nm output (ca. 100 mW) focused on a Ti/Sapphire crystal to generate a white-light continuum spectrum covers the wavelength from 420 to 800 nm. The pump and probe beams were focused onto the sample and meanwhile kept the temporal and spatial overlap at the sample. A cell with a 2 mm optical path length with a stir bar was used to keep the sample fresh and even. The instrument response function of this system was determined to be 150 fs.

2.6. Computational methods and details

All the computations were implemented with spin-polarized density

functional theory (DFT) method, as performed by the Vienna ab initio simulation package (VASP)[27]. The projector augmented wavefunction (PAW) pseudo-potentials are used to describe ionic potentials[28]. The exchange correlation energy is described by Perdew–Burke–Ernzerhof (PBE) functional within the generalized gradient approximation (GGA) [29]. In the course of the geometry relaxation, the energy cut-off was chosen as 400 eV. The DFT-D3 semiempirical correction was described via Grimme's scheme method for the single layer g-C₃N₄. In structural optimizations, the Brillouin zone are sampled by $3 \times 3 \times 1$ mesh points in k-space based on Monkhorst-Pack scheme for the samples' structures. The vacuum gap is set as 15 Å to preclude interplay between two adjacent surfaces. The convergence criterion for the iteration in self-consistent field (SCF) and the force convergence criterion for atomic relaxation are set to be 10⁻⁵ eV and 0.01 eV/Å, respectively.

3. Results and discussion

3.1. Materials characterizations

The synthetic processes of BPCN were proceeded by two steps of thermal polymerization as shown in Fig. 1a. Briefly, in step I, the CN and PCN were synthesized by conventional thermal polycondensation of melamine and diammonium hydrogen phosphate in a Muffle furnace, respectively. Then, the BCN and BPCN were obtained by the calcination of sodium borohydride as the B source combined with the CN and PCN in a tube furnace under a nitrogen atmosphere at 400 °C (Step II), respectively. As shown in Fig. 1b, the representative transmission electron microscopy (TEM) image of the bulk CN showed the large aggregates which were composed of the irregularly stacked flakes. The PCN have the same morphology with the CN, as shown in Fig. 1c. The BCN and BPCN were comprising the clean and ultrathin nanosheets, as shown in Fig. 1d and e, respectively. Furthermore, the energy dispersive X-ray spectrometry (EDX) elemental mapping of BPCN (Fig. 1f) showed that C, N, B and P were homogeneously distributed in the ultrathin g-C₃N₄, indicating the successful doping of multiple elements. The atomic force microscopy (AFM) image of the BPCN (Fig. 1g) displayed the typical sheet-like BPCN. The thickness of the BPCN was measured as 1.5 nm based on the corresponding height profiles of the AFM result, indicating the BPCN contained 4–5 layers according to the theoretical interlayer distances of g-C₃N₄ (~ 0.35 nm) (Fig. 1h).

3.2. Structural characterizations

Powder X-ray diffraction (XRD) measurements were performed to investigate the effects of B, P elements doping on the crystal structures of the BPCN (Fig. 2a). Typically, in bulk CN, the diffraction peak at 13.1° (2θ) was originated from the in-plane structural packing motif of aromatic rings and the peak at 27.6° (002) corresponding to the interlayer-stacking of the g-C₃N₄ layered structure.[30,31] The intensity of (002) peak of the BPCN significantly decreased as shown in the inset of Fig. 2a, indicating that the layered g-C₃N₄ could be stripped into ultrathin lamella-layers[32], which was consistent with TEM and AFM image observations. This peak in the PCN was shifted to the low angle, while the high angle shift in the BCN, indicated that the elements were doped in the lattices. In addition, the peak of the BPCN was slightly shifted to the low angle, suggesting that B, P could be codoped in the crystal lattices of CN. Furthermore, the N₂ absorption-desorption curves of CN and BPCN were measured (Fig. 2c). It could be found that both curves gave the typical IV hysteresis loops and pore-size distribution diagrams based on the Barrett–Joyner–Halenda (BJH) method, suggesting the existence of a mesoporous structure[5]. Notably, the surface area of the BPCN (123.2 m² g⁻¹) was almost twice of bulk g-C₃N₄ (56.3 m² g⁻¹), which could provide more active sites for enhancing photocatalytic activity.

The chemical structures of the BPCN were further investigated by the Fourier transform infrared spectroscopy (FT–IR) spectra (Fig. 2b). The characteristic vibration bands at 1200–1700 cm⁻¹ were from the stretching modes of the C–N and C≡N vibrations[33]. Furthermore, the sharp peak centered at 800 cm⁻¹ corresponded to the intrinsic heptazine unit of the g-C₃N₄ structure[34]. In addition, the broad absorption bands at 3000–3400 cm⁻¹ were attributed to the absorbed H₂O molecules and the uncondensed amino group[35]. It was proved that the BPCN retains the structure of CN in the graphic phase.

3.3. XPS analysis

The X-ray photoelectron spectroscopy (XPS) measurements were conducted in combination with density functional theory (DFT) calculations to identify the doping sites of B and P in the BPCN. Firstly, to clarify the B and P substitution sites in the CN, the theoretical calculations were used to be evaluated by the Vienna Ab initio Simulation Package (VASP) software. The corresponding atomic schemes of the B and P-doped CN, respectively, with all kinds of the energetic configurations were shown in Fig. S1. As shown in Fig. S1a, it was the model

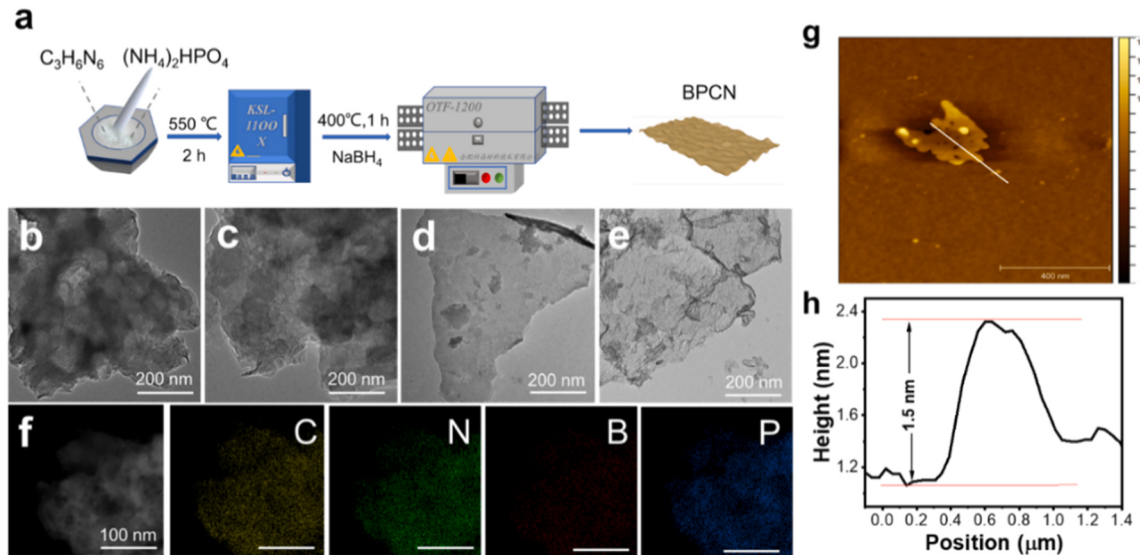


Fig. 1. (a) Schematic illustration of the synthesis processes of the BPCN; Representative TEM images of (b) bulk CN, (c) PCN, (d) BCN, (e) BPCN; (f) TEM-EDS elemental mapping images of the BPCN. Scale bars: 100 nm; (g) The representative AFM images and (h) corresponding height profiles of the BPCN.

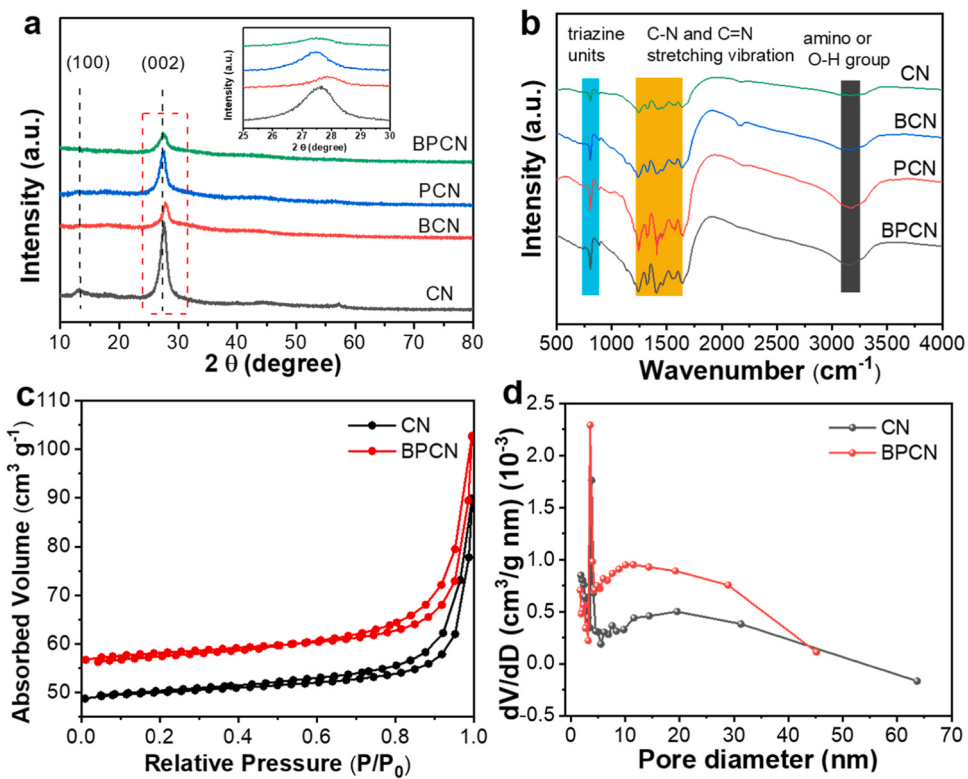


Fig. 2. (a) XRD patterns, the insert picture is the enlarged by the red dashed rectangle, (b) FT-IR spectra of BPCN, PCN, BCN and CN. (c) The N_2 absorption-desorption isotherms, (d) Pore distribution diagram of the CN and BPCN.

diagram of different C and N sites in the pristine CN. It was noted that the formation energy E_f of C2 sites replaced by the P in CN ($E_f = -5.64$ eV) was the smallest among that of all possible sites of P-doped CN, as shown in Fig. S1b[36]. The P atoms were preferentially located at the three P-N coordinates. In addition, as shown in Fig. S1c, the formation

energy E_f ($E_f = -3.26$ eV) at the N_2 position replaced by the B in the $g\text{-C}_3\text{N}_4$ was the most negative among numerous doping substitution sites, indicating that B could replace the N site forming the $C=N-C$. Notably, when the B and P were co-doped, the formation energy ($E_f = -469.0$ eV) of C1 sites replaced by the P and N2 sites replaced by the B in

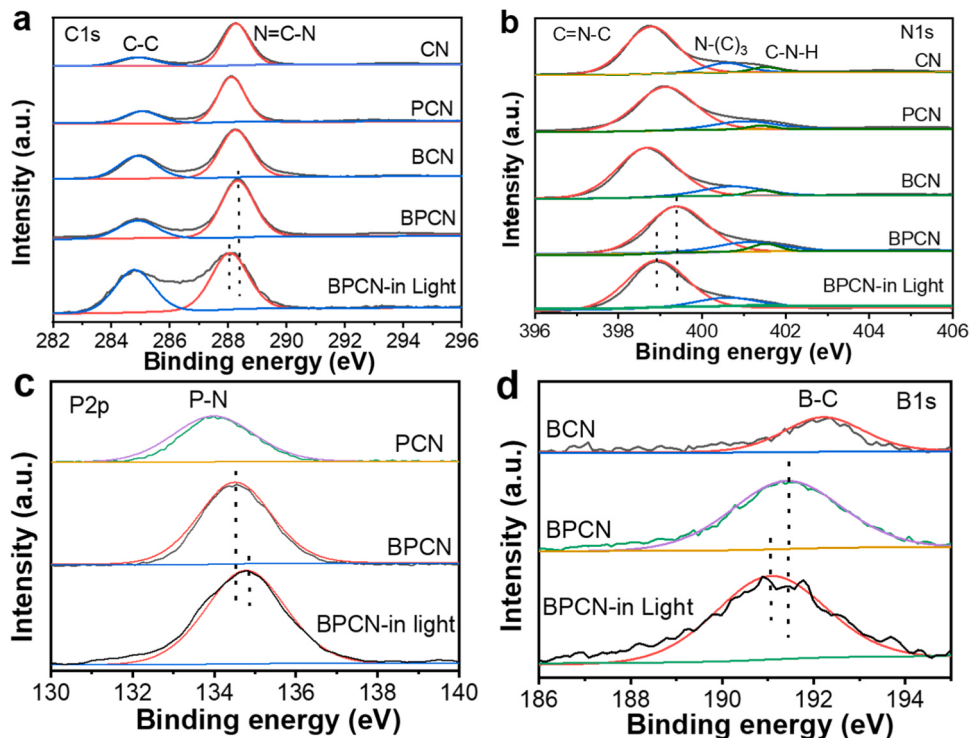


Fig. 3. The XPS (In-situ and ex-situ) spectra of (a) C 1s; (b) N 1s; (c) P 2p; (d) B 1s for CN, PCN, BCN and BPCN.

the heterocyclic CN was lowest among that of all possible sites of B, P-doped CN as shown in Fig. S1d. As a result, the P and B in BPCN could replace the C1 sites and N2 sites of CN forming the P–N and B–C coordination bonds, respectively.

The high resolution C 1s spectra (Fig. 3a) of the four samples could be fitted into two peaks at binding energies of 284.8 and 288.3 eV, which could be assigned to graphitic carbon (C–C coordination) and sp^2 -hybridized carbon (N–C=N), respectively[37]. Notably, compared with CN, the peak positions at 288.32 eV (N–C=N) of BCN and BPCN were shifted to the direction of the low binding energy. It was attributed to the less electronegative of electron-deficient B than that of N. As shown Fig. 3b, the N 1s spectra displayed C–N=C bonding, tertiary N bonds in N–(C)₃ groups and C–N–H functional group at 398.51, 399.85 and 401.04 eV, respectively[38,39]. Compared with CN, the peak positions of PCN and BPCN at 398.51 eV (C–N=C) were shifted towards the direction of higher binding energy, resulting from the fact that electron-rich P with high electronegativity could replace C in CN to form a coordination bond between P–N leading to the decrease of the charge distribution around N. As shown in Fig. 3c, we could observe an obvious peak at 134.0 eV of the P 2p orbitals in PCN, which was assigned to the P–N coordination bond. While in BPCN, the P–N coordination bond was shifted to high binding energy of 134.5 eV [40]. The binding energy of B 1s orbital in BCN was 192.2 eV, which was assigned to the B–C coordination bond[10], as shown in Fig. 3d. In the BPCN, the binding energy at 191.4 eV of B–C coordination bond was shifted to low binding energy. Compared with PCN and BCN, the shift of P–N peak in BPCN to high binding energy and B–C peak to low binding energy may be due to the change of electron density distribution in π delocalization of carbon nitride by the incorporation of B and P. Furthermore, the in-situ XPS spectra in Fig. 3 show that in the BPCN under visible light irradiation, the peak value of P shifts to the direction of the high binding energy, while the peak value of N, C, and B shifts to the direction of the low binding energy, indicating that electron-rich P

loses electrons and transfers to electron-deficient B through the P–N–C–B pathway. These results also indicated that the electron could be transferred from the electron-rich of P atom to the electron-deficient B atom. It was consistent with the differential charge density results calculated by the following DFT calculation in Fig. 8a [41,42]. In addition, according to the percentages of C, N, P, and B determined by the XPS analysis (Table S1), the contents of N and C element in pure CN are about 53.5 atoms % and 46.5 atoms %, whereas the atomic percent of C atom was decreased from 46.5 atom % in pure CN to 40.8 atom % in PCN, and to 42.3 atom % in the BPCN, respectively. The atomic percent of N atom was decreased from 53.5 atom % in pure CN to 50.6 atom % in BCN, and to 51.2 atom % in BPCN, indicating that P and B atoms could easily replace C and N elements, respectively. The results indicated that B and P were successfully doped into the graphite carbon nitride frameworks, which were consistent with the DFT results.

3.4. Photoelectric test analysis

To explore the charge separation processes and interfacial properties between the electrode and the electrolyte, transient photocurrent responses and the electrochemical impedances spectroscopy (EIS) spectra of the samples were measured. As shown in Fig. 4a, the BPCN exhibited the highest photocurrent density ($3.8 \mu\text{A cm}^{-2}$) than that of CN ($2.2 \mu\text{A cm}^{-2}$), PCN ($2.3 \mu\text{A cm}^{-2}$) and BCN ($2.6 \mu\text{A cm}^{-2}$), indicating that the BPCN showed the efficient charge separation for the enhanced photocatalytic activity under the visible light irradiation. In addition, in the Nyquist plots of Fig. 4b, the BPCN showed the smallest semicircle radius compared to other samples, suggesting the fast charge transfer rates with the low charge-transfer resistance [24,25]. Moreover, the photoluminescence (PL) spectra and time-resolved PL spectra are powerful tools to estimate the recombination of photogenerated charge carrier transfer [43,44]. As shown in Fig. 4c, the BPCN exhibited the weakest PL intensity at the peak of 465 nm than that of CN, PCN and BCN,

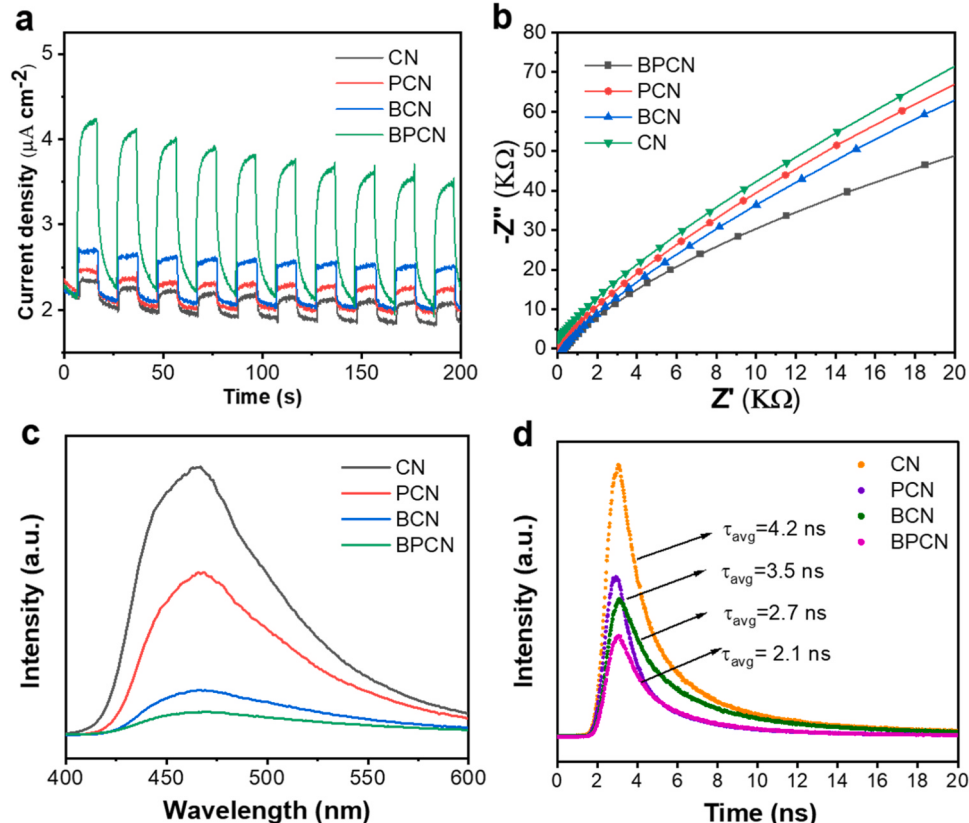


Fig. 4. (a) Photocurrent-time response profiles, (b) electrochemical impedance spectra, (c) steady-state and (d) time-resolved PL spectra of CN, PCN, BCN and BPCN.

indicating more efficient separation of the charge carriers. Time-resolved PL spectra (Fig. 4d) showed that the average lifetime (2.1 ns) for the BPCN was lower than that of other three samples, implying the fast electron-hole separation and transport in the BPCN. Thus, the BPCN exhibited high efficient charge separation favoring the high photocatalytic activity.

3.5. Optical absorption and band structures

To explore the functions of introducing non-metal B, P atoms in g-C₃N₄ affecting the band structures, the hybrid functional theory (HSE) calculation was used to obtain the theoretical density of states (DOS). According to the results of DOS, the band gap of pure CN was about 2.54 eV as shown in Fig. 5a, which was consistent with reported results [45]. By calculating the DOS of the optimized B, P-doped sites structures in g-C₃N₄ in Fig. S1, the band gaps of the BCN and PCN were estimated to be 2.11 eV and 2.23 eV, respectively, in Figs. 5b and 5c. Due to the interactions between non-metallic elements, the band gap value of the BPCN was 2.20 eV which was located between PCN and BCN, as shown in Fig. 5d. It could be concluded that the when the non-metal elements doped in the g-C₃N₄, the narrower band gaps were obtained, which could absorb the wide range of visible light for improving the photocatalytic performance. Furthermore, the conduction band (CB) of the BPCN was closer to the Fermi level than that of CN, indicating that BPCN displayed a higher carrier density and better charge transfer capability [46]. Beside theoretical calculation, we also used the UV-vis diffraction reflectance spectroscopy (DRS) spectra, Mott-Schottky profiles to determine the band structures diagrams. The UV-vis DRS results in Fig. 5e showed that the absorption band edges of CN. The PCN, BCN and BPCN showed an obvious redshift and increased absorption intensity, indicating an increased harvesting of visible light. The band gaps of

samples were estimated to be 2.70, 2.62, 2.59 and 2.46 eV for CN, PCN, BCN and BPCN, respectively, as shown in Fig. 5f, according to the Kubelka-Munk function transformation. In order to clarify the band structure of CN, PCN, BCN and BPCN, the flat-band potentials and charge carrier concentrations were calculated according to the Mott-Schottky plot in Fig. 5g. The Mott-Schottky equations were following:

$$\frac{1}{C^2} = \left(\frac{2}{N_D e_0 \epsilon \epsilon_0} \right) \left[(E - E_{FB}) - \frac{kT}{e_0} \right] \quad (2)$$

$$N_D = \frac{2}{e \epsilon_0 \epsilon} \left(\frac{dE}{d\left(\frac{1}{C^2}\right)} \right) \quad (3)$$

where C, ND, E and E_{FB} were the charge capacitance, carrier density, applied potential and flat band potential, respectively; e₀, ϵ and ϵ_0 refer to the charge constant (1.60×10^{-19} C), dielectric constant (7–8 for g-C₃N₄) and permittivity of a vacuum (8.85×10^{-12} F m⁻¹); k is the Boltzmann constant (1.38×10^{-23} J K⁻¹); and T is the temperature. After calculation, the ND value of the BPCN (9.2×10^{19} cm⁻³) was the highest among those of the CN (3.2×10^{19} cm⁻³), PCN (4.5×10^{19} cm⁻³) and BCN (5.3×10^{19} cm⁻³), which indicated the efficient separation of the charge carriers to produce more active electrons for hydrogen production. The value of the flat band potential was defined by $1/C^2 = 0$. The E_{FB} of CN, PCN, BCN and BPCN were determined to be -1.12 , -1.25 , -1.31 and -1.42 V vs Ag/AgCl. For n-type semiconductors, the E_{FB} was 0.1–0.2 eV higher than conduction band(CB) [30]. To estimate the CB position of the photocatalyst, the potential difference between CB and E_{FB} was set at 0.2 eV. So the potentials of CB for CN, PCN, BCN and BPCN were estimated to be about -1.32 , -1.45 ,

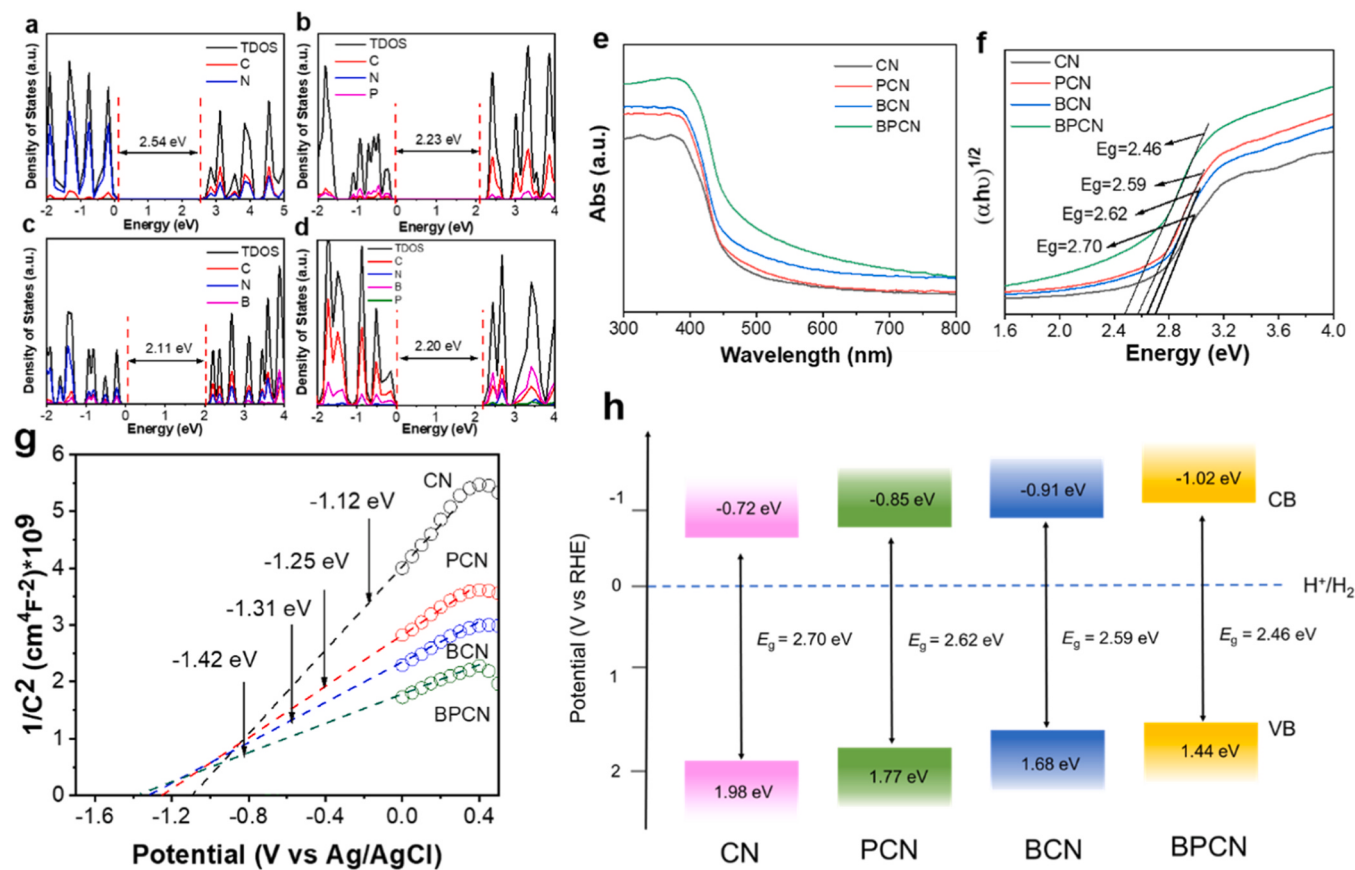


Fig. 5. Density of state (DOS) spectra of (a) pristine CN, (b) PCN, (c) BCN, (d) BPCN. (e) UV-visible absorbance spectra, (f) Mott-Schottky plots and (g) energy level diagrams of CN, PCN, BCN and BPCN. CB: conduction band; VB: valence band.

– 1.51 and – 1.62 V vs Ag/AgCl, which were equivalent to – 0.72, – 0.85, – 0.91 and – 1.02 V vs RHE. The corresponding valence band (VB) values were about 1.98, 1.77, 1.68 and 1.44 eV. The corresponding band structure diagram of the samples was shown in Fig. 5h. The CB potential of BPCN was smaller than that of other samples and was more negative compared with the H⁺/H₂ reduction potential (NHE). Thus, the up-shift of conduction band energy could result in a stronger reducing activity of the BPCN, leading to a significant improvement in photocatalytic HER.

The band-gap energy (E_g) of as-obtained samples was calculated by the Tauc plots, following the equation [46]:

$$\alpha h\nu = A(h\nu - E_g)^n/2 \quad (4)$$

where α , h , ν , A , and E_g are absorption coefficients, the Planck constant, light frequency, a constant, and the band gap energy, respectively. The value of exponential n is determined by the type of semiconducting band gap (direct band gap $n = 1$, indirect band gap $n = 4$, respectively). The Mott-Schottky (MS) measurements were performed to determine the Fermi energy levels (E_F) of materials. The potential vs. RHE was calculated using the following equation[47]:

$$E_{\text{FVS RHE}} = E \text{ vs Ag/AgCl} + 0.1976 + 0.059 \times \text{pH} \quad (5)$$

The corresponding band structures of materials are derived according to the relationships between the valence bands, conduction bands and the band gaps of the materials using the following formula:

$$E_{\text{VB}} = E_{\text{CB}} + E_g \quad (6)$$

3.6. Photocatalytic activity in HER

To determine the dual elements doping effects on the photocatalytic activity in HER, we investigated the photocatalytic hydrogen production and stability of the BPCN using the triethanolamine (TEOA) as the hole scavenger under visible-light ($\lambda > 420$ nm) irradiation. Firstly, as shown in Fig. 6a, the H₂ evolution rate of the g-C₃N₄ increased with the increase

of the P doping concentration, and the PCN exhibited HER rate of 1346 $\mu\text{mol g}^{-1} \text{h}^{-1}$, with optimum P doping contents (0.5 g P precursor), which was about 9.3 times than that of bulk CN. When the optimal molar ratio of B and P co-doping was 3:2, the photocatalytic HER rate of BPCN1.5 (namely BPCN) was the highest at 4579 $\mu\text{mol h}^{-1} \text{g}^{-1}$. As displayed in Fig. 6c, the BPCN exhibited higher photocatalytic activity in HER than that of BCN (2310 $\mu\text{mol h}^{-1} \text{g}^{-1}$), PCN (1346 $\mu\text{mol h}^{-1} \text{g}^{-1}$), ultrathin g-C₃N₄-ECN (538 $\mu\text{mol h}^{-1} \text{g}^{-1}$) and bulk CN (145 $\mu\text{mol h}^{-1} \text{g}^{-1}$). We also did the time-evolved photocatalytic activity in HER of BPCN, PCN, BCN and CN, as shown in Fig. 6d. The total amount of H₂ of BPCN reached 19.1 mmol after 4 h. The stability was another key factor to evaluate the photocatalysts. After five cycling tests, the BPCN still exhibited excellently stable photocatalytic activity in HER after 15 h, as shown in Fig. 6e. The morphology and structural information of the BPCN after photocatalytic HER were maintained without any obvious change, as shown in Figs. S2 and S3, respectively. To further obtain the photocatalytic HER proceeded of the BPCN through photoexcitation of the light absorption, we investigated the relationship between the photocatalytic AQY of HER and wavelengths of incident light. As displayed in Fig. 6f, the AQY values were reproduced and matched well with the absorption spectrum. The AQY of the BPCN was 19.6% at 400 nm, which outperformed in the g-C₃N₄-based catalysts reported in the literatures (Table S4). These results indicated that the BPCN exhibited remarkably high and stability photocatalytic activity in HER.

3.7. Photoinduced carrier dynamics

To understand the intrinsic photocatalytic carrier dynamics and charge transfer routes, we performed the femtosecond transient absorption (fs-TA) spectroscopy measurements using the 400 nm laser to excite the samples. As illustrated in Figs. 7a and 7b, the broad negative absorption band (from 450 to 800 nm) was only observed for the CN, mainly due to stimulated emission (SE) or the state filling of photo-bleaching [48]. However, the BPCN displayed two polarized characteristic absorption areas at (i) 450–640 nm (negative absorption) and (ii) 640–800 nm (positive absorption), respectively, as shown in Figs. 7d and 7e. The features with the negative signal were due to the ground

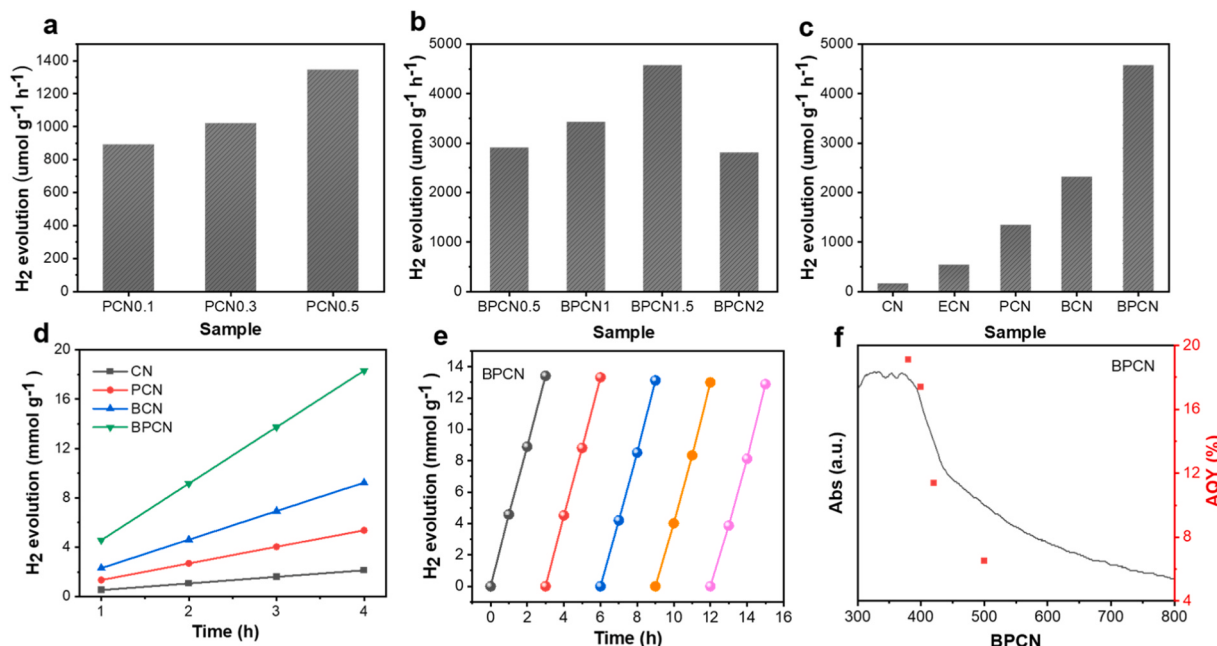


Fig. 6. Photocatalytic H₂ generation rates of (a) different doping amounts of P in g-C₃N₄, (b) different codoping amounts of B and P in g-C₃N₄ under visible-light irradiation ($\lambda > 420$ nm). (c) Comparison of photocatalytic activity in HER of the CN, ECN, PCN, BCN and BPCN. (d) Time-evolution photocatalytic hydrogen evolution of the as-obtained photocatalysts. (e) The cycling tests of the BPCN. (f) Photocatalytic apparent quantum yield in HER of the BPCN under different single wavelengths and the absorption spectrum of the BPCN.

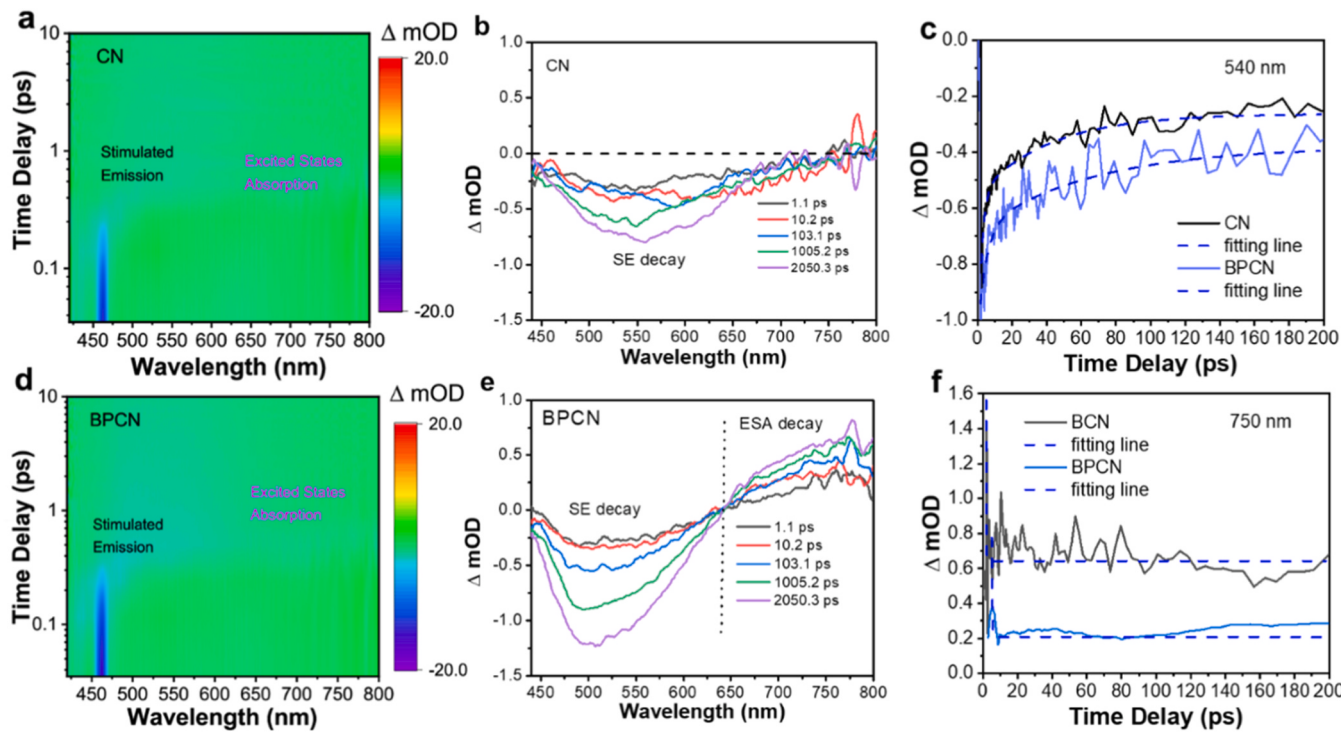


Fig. 7. Time-dependent contour plots of femtosecond TA spectra (TAS) (pump laser: 400 nm): (a) CN, (d) BPCN; The TAS of (b) CN, (e) BPCN. Kinetics decay profiles of the CN and BPCN at 540 nm (c), the BCN and BPCN at 750 nm (f), respectively. Best fits were in blue lines.

state bleaching or stimulated emission (SE) [49] and the positive signal was assigned to the excited-state absorption (ESA) [50–52]. Because the UV-Vis DRS and steady-state PL spectra of the CN clearly showed the band edge absorption before 450 nm and the strong intensity of the emission peak at 450 nm, respectively, the negative absorption feature could be attributed to the SE. The ESA feature in the visible-light region was primarily caused by photoinduced electrons in the CN [53–56]. Compared with the PCN in Figs. S4a, 4b, and the CN, the TA spectra (TAS) of the BCN and BPCN showed the remarkable enhancement in the ESA region, while the PCN only a little and ignorable intensity of ESA signal. It indicated that the electron-deficient B in g-C₃N₄ could induce the fast charge separation for enhanced photocatalytic activity.

The kinetic decay traces of the photoinduced carriers of the CN and BPCN were plotted and probing at SE (540 nm), as shown in Fig. 7c. The biexponential decay functions were employed to fit the photo-excited carrier dynamics. For the pristine CN, the one component (τ_1) was ascribed to the electron shallow trapping at the time constant of 4.72 ps, as shown in Table S2. The other component of τ_2 (41.6 ps) was attributed to the recombination of the shallow trapped electron with the hole on valence band (VB). Compared with the CN, the fast charge trapping component ($\tau_1 = 2.16$ ps) of the BPCN could favor the efficient charge separation. The slower recovery ($\tau_2 = 65.7$ ps) indicated the long lifetime for increasing the active electron transport for the photocatalytic HER.

In order to further analyze the electron trapping dynamics of electron-deficient B in a shallow trap state under ESA. The kinetic dynamical decay traces of the photoinduced-excited carriers of the BCN and BPCN were plotted and probing at ESA (750 nm), as shown in Fig. 7f. The corresponding exponential fitted parameters are listed in Table S3. For the BCN, two-exponential decay function was used and the components can be ascribed to the initial shallow electron trapping ($\tau_1 = 0.8$ ps) and photogenerated electron-hole pair recombination ($\tau_2 = 8.0$ ps). Compared with the BCN, the BPCN proceeded the fast charge trapping ($\tau_1 = 0.3$ ps) and exhibited much long lifetime of the electron-hole charge separation ($\tau_2 = 31$ ps). Furthermore, the kinetic dynamical decay traces of the photoinduced-excited carriers of the CN and PCN

were plotted and probing at the probing wavelength (750 nm), as shown in Fig. S4f. The corresponding exponential fitted parameters are listed in Table S3. For the CN, we could clearly observe the features with a broad negative signal up to 750 nm due to the ground state bleaching or stimulated emission (SE). Thus, the initial shallow electron trapping didn't exist. However, for the PCN, the ESA signal at 750 nm could be obviously observed and the decay profiles could be fitted by the biexponential functions. Two components have been assigned to the the fast shallow electron trapping ($\tau_1 = 0.38$ ps) and the recombination of the electron-hole ($\tau_2 = 21$ ps), as listed in Table S3. Generally, the photo-generated electrons in the g-C₃N₄ could easily fall into deep trap states, followed by photoactivity quenching, as previously reported by Durrant [57–59]. Thus, the above results indicated that the electron-rich P and electron-deficient B acted as electron donors and acceptors in the BPCN, which synergically promoted the efficient shallow electron trapping in g-C₃N₄ and effectively inhibited the recombination of photogenerated electrons and holes.

3.8. Theoretical calculation

Furthermore, the DFT calculations were used to understand the excellent performance in HER of the BPCN. As shown in Fig. 8a, the differential charge density diagrams showed the charge distributions of the CN, PCN, BCN and BPCN, in which the yellow and cyan regions represented electron accumulation and depletion, respectively. From the Bader charge analysis, for the PCN, the charge transfer was from the P to N due to the high electronegativity of N, resulting into the Bader charge increase of N from 6.18 to 6.31, compared with the CN. In the BCN, the Bader charge of B was 1.32. When B and P both doped in CN, the Bader charge of B was increased to 6.23. It indicated that the electrons at the electron-rich P sites could be transferred to the electron-deficient B sites as an electron donor through the P→N→C→B electron transport channel. To further analyze the contribution of the orbitals of the P and B to the band structures, the local density of state spectra were used. The VB of pure CN was mainly composed of the N 2p_z orbitals, and the conduction band (CB) was mainly comprising the C 2p_y orbitals, as

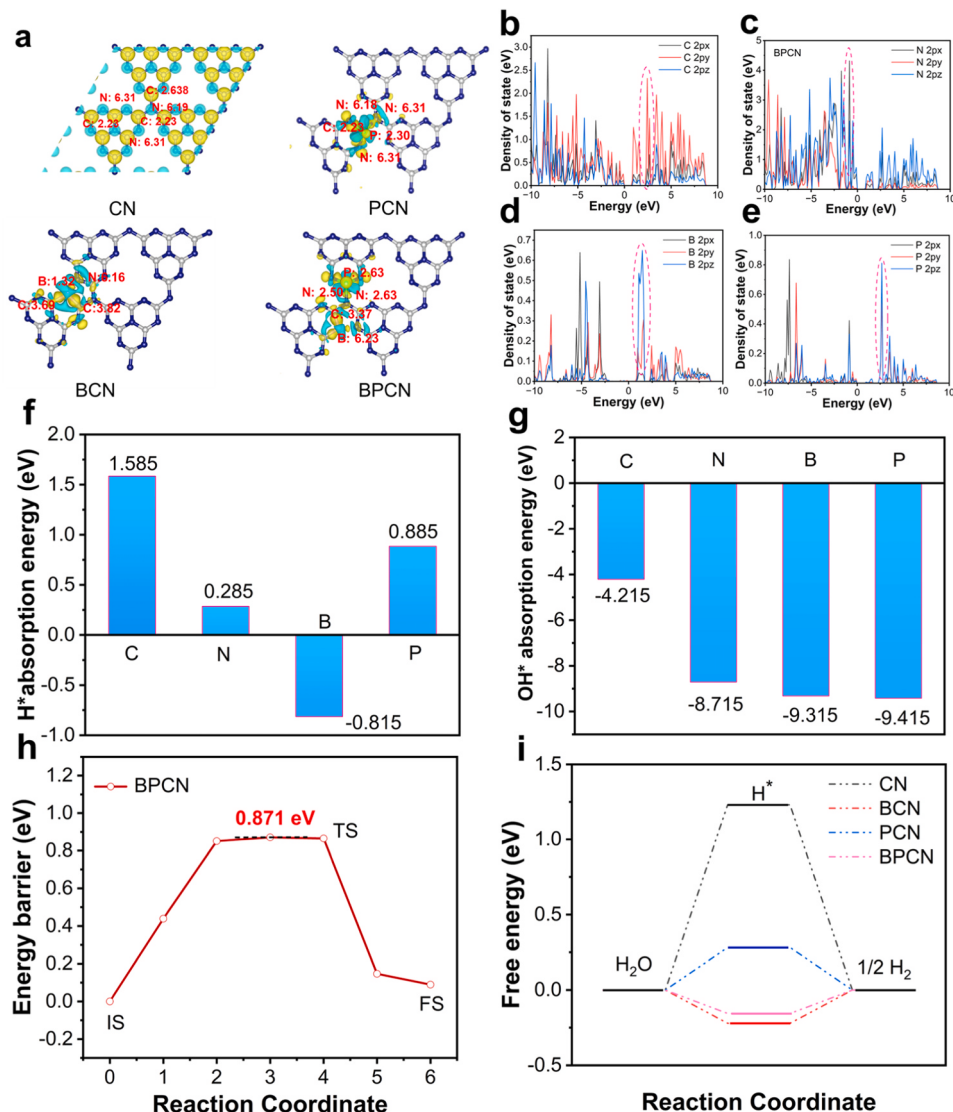


Fig. 8. (a) Charge density difference maps of the as-obtained samples. The yellow and cyan regions represented the electron accumulation and depletion, respectively. The values at the atoms were the Bader charge. (b-e) The calculated local density of states (DOS) of the BPCN. Absorption energy of different elements with (f) hydrogen (H^*) and (g) hydroxyl (OH^*) on the BPCN. (h) Transition state diagram of water splitting on the BPCN. (i) Free energy profiles of hydrogen absorption over the CN, PCN, BCN and BPCN for HER.

shown in Fig. S5. As shown in Fig. S6, the VB of the PCN was mainly composed of N 2pz and P 2pz orbitals. However, the CB of the BCN was mainly comprising the C 2py and B 2pz (Fig. S7). For the BPCN in Fig. 8b–e, the CB was composed of C 2py, P 2pz, and B 2pz orbitals, and the VB was mainly composed of N 2pz and P 2pz orbitals. When pure CN was excited by the visible light, it was difficult for electrons to be transferred from the N 2pz to the C 2py orbital due to the different orbital polar directions. For the BPCN, the electron transition could take a much easier pathway in the same plane from N 2pz to B 2pz by the excitation. In pure CN, the excited electrons (from the N atom orbital to the C atom orbital) could be recombined with the photogenerated holes by the reverse approach to reduce the photocatalytic reaction with the N as the active sites, which was an important reason for the high photo-induced carrier recombination rates in the C–N heterocyclic plane [60, 61]. For the BPCN, the electron-rich P 2pz at the VB could be acted as the electron pump. After photoexcitation, the excited electrons could be transferred to the B 2pz sites at the CB due to the high overlapping of the electron density and the same plane favouring the electron transfer from the P 2pz to the B 2pz. Therefore, combined with the Bader charge results, it could be proved that in BPCN, the electron transfer in the π

off-domain was from P 2pz in the VB to N 2pz with strong electronegativity, and after photoexcitation, the photogenerated electrons were transferred from the VB to B 2pz in the CB. The B 2pz at the CB could promote the fast capture of the electron in the shallow trapping state, reducing the recombination of photoinduced electron-hole pairs for enhanced photocatalytic activity.

Furthermore, to reveal the mechanism of the photocatalytic HER, the absorption energies of different elements on the BPCN for water splitting radicals H^* and OH^* are simulated and calculated. As shown in Figs. 8f and 8g and S8, compared with absorption active sites on the BPCN, the absorption energy of element B for H^* was the lowest (-0.815 eV), and that of element P for OH^* was the lowest (-9.415 eV). Therefore, the absorption processes of H^* and OH^* at B and P sites, respectively, are more likely to occur. It further indicated that the B could effectively absorbed H^* and the P absorbed OH^* , so the B and P played a synergistic role for the water splitting. In addition, to investigate the processes of water splitting on the BPCN, we also calculated the processes of the transition state. As shown in Fig. 8h and Fig. S9, the activation energy required for the initial absorption of H_2O molecules on P, the decomposition of H_2O to form H – OH (H on B and OH on P) was only 0.871 eV.

According to the diagram of hydrogen overflow during water splitting on the surface of the BPCN in Fig. S9, it can be clearly seen that H_2O molecules are first absorbed at the P site, then cleaved to H-OH , released the protons, and finally absorbed at the B site. Therefore, the preferential absorption of H_2O at the P site followed by the hydrogen spillover at the B site could occur. Therefore, it could be concluded that the BPCN exhibited high efficiency of photocatalytic HER. Furthermore, the reactions of the hydrogen absorption on photocatalysts also played the pivotal role in the photocatalytic HER. The Gibbs free-energy of atomic hydrogen absorption, $|\Delta G_{\text{H}^*}|$, has been considered as a reasonable descriptor of the HER activity. As shown in Fig. 8i, the ΔG_{H^*} value of the CN was 1.23 eV, which was not favourable for the photocatalytic HER. However, the ΔG_{H^*} value of the BCN (0.22 eV) was smaller than that of the PCN (0.28 eV), indicating that the BCN has high photocatalytic activity which was consistent with the results of the photocatalytic HER part. Notably, the ΔG_{H^*} value of the BPCN was 0.16 eV, which was closer to 0 eV, which was more conducive to the absorption and desorption processes of the active hydrogen, favouring the high photocatalytic hydrogen production.

3.9. The mechanism of photocatalytic activity in HER

The photocatalytic enhancement mechanism in HER of the BPCN was proposed as shown in Fig. 9. First, the smaller band gap of the BPCN could expand the light absorption range and provided more carrier density for photocatalytic activity. The high value of the CB also gave the high reduction ability for HER. Secondly, since the electronegativity of the N was greater than the P, the electron-rich P could transfer the electron to the N through a new charge transfer channel ($\text{P} \rightarrow \text{N} \rightarrow \text{C} \rightarrow \text{B}$). The electron transition could take a much easier pathway in the same plane from N 2pz to electron deficient B 2pz on the CB under the visible light excitation for the efficient electron shallow trapping state. The synergistic effects of the B and P could promote the efficient separation of photogenerated carriers. According to the calculation of absorption energy and transition state on the BPCN, the strong absorption of the P to OH^* and B to H^* occurred through the H_2O pyrolysis. The phenomenon of the hydrogen spillover was produced from the P to the B sites which were considered as the active sites for the HER. Therefore, the high photocatalytic activities in HER of the BPCN were attributed to the synergistic effects of the B and P codoping, the hydrogen spillover processes and a new charge transfer pathway ($\text{P} \rightarrow \text{N} \rightarrow \text{C} \rightarrow \text{B}$).

4. Conclusions

In summary, we successfully synthesized the simultaneous B and P codoping the CN forming the ultrathin BPCN nanosheets with a thickness of ~ 1.5 nm by the sequential annealing methods. The BPCN exhibited higher photocatalytic activity in HER than that of CN, PCN and BCN. The AQY of the BPCN is 11.4% at 420 nm and 19.1% at 380 nm superior to most reported g-C₃N₄-based catalysts. Theoretical calculations and TAS measurements provided the evidence that the remarkable photocatalytic activity and excellent stability of the BPCN were attributed to the a new charge transfer pathway ($\text{P} \rightarrow \text{N} \rightarrow \text{C} \rightarrow \text{B}$) and the efficient shallow electron trapping through the electron transfer from the electron-rich P at the VB to the electron-deficient B, prolonging the lifetime of photogenerated carrier charge separation. Meanwhile, the P site strongly absorbed the H_2O and then cracked to form the H-OH . The H^* then overflowed to the B site as the active sites for the efficient photocatalytic hydrogen production to achieve an effective hydrogen spillover pathway. The synergistic effects of B and P elements in the π separation domain of carbon nitride in BPCN provides a promising strategy for the conversion of solar energy into hydrogen energy by promoting the efficient separation of photogenerated carriers and the hydrogen spillover pathway.

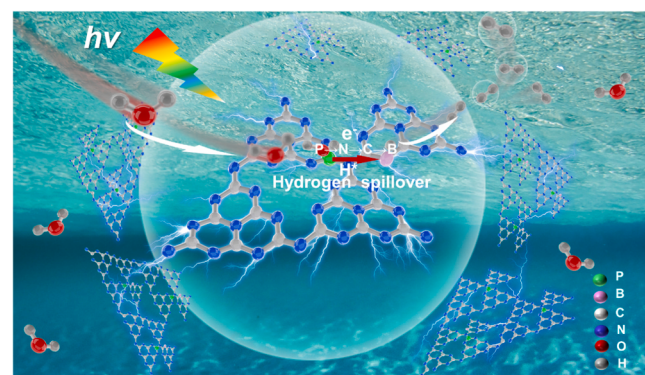


Fig. 9. The proposed mechanism for photocatalytic HER over the BPCN.

CRediT authorship contribution statement

Fangfang Gao and Han Xiao equally contributed to this work. **Fangfang Gao:** Formal analysis, Data curation, Software, Writing-original draft. **Han Xiao:** Investigation, Calculation. **Jiarui Yang:** Data curation. **Xue Luan, Duoduo fang:** Software, Validation. **Lei Yang:** Validation. **Jiangzhi Zi:** Investigation, Writing-review & editing. **Zichao Lian:** Conceptualization, Funding acquisition, Writing-review & editing.

Declaration of Competing Interest

The authors declare that they have no known competing financial interests or personal relationships that could have appeared to influence the work reported in this paper.

Data Availability

Data will be made available on request.

Acknowledgments

This work was supported by the National Natural Science Foundation of China (22109097), and the Natural Science Foundation of Shanghai (20ZR1472000).

Appendix A. Supporting information

Supplementary data associated with this article can be found in the online version at doi:10.1016/j.apcatb.2023.123334.

References

- [1] Z. Lian, Y. Kobayashi, J.J.M. Vequito, C.S.K. Ranasinghe, A. Yamakata, T. Nagai, K. Kimoto, K. Kobayashi, N. Tamai, T. Teranishi, M. Sakamoto, Harnessing infrared solar energy with plasmonic energy upconversion, *Nat. Sustain.* 5 (2022) 1092–1099.
- [2] Z. Lian, M. Sakamoto, J.J.M. Vequito, C.S.K. Ranasinghe, A. Yamakata, T. Nagai, K. Kimoto, Y. Kobayashi, N. Tamai, T. Teranishi, Plasmonic p-n junction for infrared light to chemical energy conversion, *J. Am. Chem. Soc.* 141 (2019) 2446–2450.
- [3] Z. Lian, F. Wu, Y. Zhong, J. Zi, Z. Li, X. Wang, T. Nakagawa, H. Li, M. Sakamoto, Tuning plasmonic p-n junction for efficient infrared-light-responsive hydrogen evolution, *Appl. Catal. B: Environ.* 318 (2022) 121860.
- [4] Z. Li, J. Zi, X. Luan, Y. Zhong, M. Qu, Y. Wang, Z. Lian, Localized surface plasmon resonance promotes metal–organic framework-based photocatalytic hydrogen evolution, *Adv. Funct. Mater.* 2303069 (2023).
- [5] Z. Lian, M. Sakamoto, H. Matsunaga, J.J.M. Vequito, A. Yamakata, M. Haruta, H. Kurata, W. Ota, T. Sato, T. Teranishi, Near infrared light induced plasmonic hot hole transfer at a nano-heterointerface, *Nat. Commun.* 9 (2018), 2314.
- [6] Y. Zhong, J. Zi, F. Wu, Z. Li, X. Luan, F. Gao, Z. Lian, Defect-mediated electron transfer in Pt–CuInS₂/CdS heterostructured nanocrystals for enhanced photocatalytic H_2 evolution, *ACS Appl. Nano Mater.* 5 (2022) 7704–7713.

[7] J. Sun, R. Malishev, A. Azoulay, J. Tzadikov, M. Volokh, R. Jelinek, M. Shalom, Carbon and nitrogen based nanosheets as fluorescent probes with tunable emission, *Small* 14 (2018), 1800516.

[8] O. Elbanna, M. Zhu, M. Fujitsuka, T. Majima, Black phosphorus sensitized TiO_2 mesocrystal photocatalyst for hydrogen evolution with visible and near-infrared light irradiation, *ACS Catal.* 9 (2019) 3618–3626.

[9] J. Zi, Y. Zhong, Z. Li, F. Wu, W. Yang, Z. Lian, Type-I CdSe/ZnS heteronanoplatelets exhibit enhanced photocatalytic hydrogen evolution by interfacial trap-mediated hole transfer, *J. Phys. Chem. C* 125 (2021) 23945–23951.

[10] Z. Lian, Z. Li, F. Wu, Y. Zhong, Y. Liu, W. Wang, J. Zi, W. Yang, Photogenerated hole traps in metal-organic-framework photocatalysts for visible-light-driven hydrogen evolution, *Commun. Chem.* 5 (2022) 93.

[11] A. Savateev, I. Ghosh, B. König, M. Antonietti, Photoredox catalytic organic transformations using heterogeneous carbon nitrides, *Angew. Chem. Int. Ed.* 57 (2018) 15936–15947.

[12] X. Wang, K. Maeda, A. Thomas, K. Takanabe, G. Xin, J.M. Carlsson, K. Domen, M. Antonietti, A metal-free polymeric photocatalyst for hydrogen production from water under visible light, *Nat. Mater.* 8 (2009) 76–80.

[13] A. Savateev, B. Kurpil, A. Mishchenko, G. Zhang, M. Antonietti, A “waiting” carbon nitride radical anion: a charge storage material and key intermediate in direct C–H thiolation of methylenes using elemental sulfur as the “S”-source, *Chem. Sci.* 9 (2018) 3584–3591.

[14] X. She, J. Wu, H. Xu, J. Zhong, Y. Wang, Y. Song, K. Nie, Y. Liu, Y. Yang, M.-T. F. Rodrigues, R. Vajtai, J. Lou, D. Du, H. Li, P.M. Ajayan, High efficiency photocatalytic water splitting using 2D $\alpha\text{-Fe}_2\text{O}_3/\text{g-C}_3\text{N}_4$ Z-Scheme Catalysts, *Adv. Energy Mater.* 7 (2017), 170025.

[15] H. Shao, X. Zhao, Y. Wang, R. Mao, Y. Wang, M. Qiao, S. Zhao, Y. Zhu, Synergistic activation of peroxymonosulfate by Co_3O_4 modified $\text{g-C}_3\text{N}_4$ for enhanced degradation of diclofenac sodium under visible light irradiation, *Appl. Catal. B: Environ.* 218 (2017) 810–818.

[16] Z. Jiang, W. Wan, H. Li, S. Yuan, H. Zhao, P.K. Wong, A hierarchical Z-scheme $\alpha\text{-Fe}_2\text{O}_3/\text{g-C}_3\text{N}_4$ hybrid for enhanced photocatalytic CO_2 reduction, *Adv. Mater.* 30 (2018), 1706108.

[17] S.A. Shevlin, Z.X. Guo, Anionic dopants for improved optical absorption and enhanced photocatalytic hydrogen production in graphitic carbon nitride, *Chem. Mater.* 28 (2016) 7250–7256.

[18] Q. Ruan, T. Miao, H. Wang, J. Tang, Insight on shallow trap states-introduced photocathodic performance in n-type polymer photocatalysts, *J. Am. Chem. Soc.* 142 (2020) 2795–2802.

[19] W. Wang, H. Zhou, Y. Liu, S. Zhang, Y. Zhang, G. Wang, H. Zhang, H. Zhao, Formation of B-N-C coordination to stabilize the exposed active nitrogen atoms in $\text{g-C}_3\text{N}_4$ for dramatically enhanced photocatalytic ammonia synthesis performance, *Small* 16 (2020), 1906880.

[20] L. Luo, Z. Gong, J. Ma, K. Wang, H. Zhu, K. Li, L. Xiong, X. Guo, J. Tang, Ultrathin sulfur-doped holey carbon nitride nanosheets with superior photocatalytic hydrogen production from water, *Appl. Catal. B: Environ.* 284 (2021), 119742.

[21] J. Fu, B. Zhu, C. Jiang, B. Cheng, W. You, J. Yu, Hierarchical porous O-doped $\text{g-C}_3\text{N}_4$ with enhanced photocatalytic CO_2 reduction activity, *Small* 13 (2017), 1603938.

[22] Y. Zeng, X. Liu, C. Liu, L. Wang, Y. Xia, S. Zhang, S. Luo, Y. Pei, Scalable one-step production of porous oxygen-doped $\text{g-C}_3\text{N}_4$ nanorods with effective electron separation for excellent visible-light photocatalytic activity, *Appl. Catal. B: Environ.* 224 (2018) 1–9.

[23] J. Ji, J. Wen, Y. Shen, Y. Lv, Y. Chen, S. Liu, H. Ma, Y. Zhang, Simultaneous noncovalent modification and exfoliation of 2D carbon nitride for enhanced electrochemiluminescent biosensing, *J. Am. Chem. Soc.* 139 (2017) 11698–11701.

[24] C. Hu, W.-Z. Hung, M.-S. Wang, P.-J. Lu, Phosphorus and sulfur codoped $\text{g-C}_3\text{N}_4$ as an efficient metal-free photocatalyst, *Carbon* 127 (2018) 374–383.

[25] G. Liu, P. Niu, C. Sun, S.C. Smith, Z. Chen, G.Q. Lu, H.-M. Cheng, Unique electronic structure induced high photoreactivity of sulfur-doped graphitic C_3N_4 , *J. Am. Chem. Soc.* 132 (2010) 11642–11648.

[26] D. Zhao, Y. Wang, C.-L. Dong, Y.-C. Huang, J. Chen, F. Xue, S. Shen, L. Guo, Boron-doped nitrogen-deficient carbon nitride-based Z-scheme heterostructures for photocatalytic overall water splitting, *Nat. Energy* 6 (2021) 388–397.

[27] G. Kresse, J. Furthmüller, Efficiency of ab-initio total energy calculations for metals and semiconductors using a plane-wave basis set, *Mater. Sci.* 6 (1996) 15–50.

[28] G. Kresse, J. Furthmüller, Efficient iterative schemes for ab initio total-energy calculations using a plane-wave basis set, *Phys. Rev. B* 54 (1996) 11169–11186.

[29] J.P. Perdew, K. Burke, M. Ernzerhof, Generalized gradient approximation made simple, *Phys. Rev. Lett.* 77 (1996) 3865–3868.

[30] Y. Zhang, T. Mori, J. Ye, M. Antonietti, Phosphorus-doped carbon nitride solid: enhanced electrical conductivity and photocurrent generation, *J. Am. Chem. Soc.* 132 (2010) 6294–6295.

[31] J. Wu, N. Li, X.-H. Zhang, H.-B. Fang, Y.-Z. Zheng, X. Tao, Heteroatoms binary-doped hierarchical porous $\text{g-C}_3\text{N}_4$ nanobelts for remarkably enhanced visible-light-driven hydrogen evolution, *Appl. Catal. B: Environ.* 226 (2018) 61–70.

[32] Y. Li, X. Liu, L. Tan, Z. Cui, X. Yang, Y. Zheng, K.W.K. Yeung, P.K. Chu, S. Wu, Rapid sterilization and accelerated wound healing using Zn^{2+} and graphene oxide modified $\text{g-C}_3\text{N}_4$ under dual light irradiation, *Adv. Funct. Mater.* 28 (2018), 1800299.

[33] J. Ran, T.Y. Ma, G. Gao, X.-W. Du, S.Z. Qiao, Porous P-doped graphitic carbon nitride nanosheets for synergistically enhanced visible-light photocatalytic H_2 production, *Energy Environ. Sci.* 8 (2015) 3708–3717.

[34] H. Che, C. Liu, G. Che, G. Liao, H. Dong, C. Li, N. Song, C. Li, Facile construction of porous intramolecular $\text{g-C}_3\text{N}_4$ -based donor-acceptor conjugated copolymers as highly efficient photocatalysts for superior H_2 evolution, *Nano Energy* 67 (2020), 104273.

[35] W. Luo, Y. Li, J. Wang, J. Liu, N. Zhang, M. Zhao, J. Wu, W. Zhou, L. Wang, Asymmetric structure engineering of polymeric carbon nitride for visible-light-driven reduction reactions, *Nano Energy* 87 (2021), 106168.

[36] X.-N. Cao, S. Lian, Y. Tong, W. Lin, L. Jia, Y. Fang, X. Wang, Fluorescent self-modified carbon nitride nanosheets as biomimetic catalases for free-radical scavenging, *Chem. Commun.* 56 (2020) 916–919.

[37] S. Lv, Y.H. Ng, R. Zhu, S. Li, C. Wu, Y. Liu, Y. Zhang, L. Jing, J. Deng, H. Dai, Phosphorus vapor assisted preparation of P-doped ultrathin hollow $\text{g-C}_3\text{N}_4$ sphere for efficient solar-to-hydrogen conversion, *Appl. Catal. B: Environ.* 297 (2021), 120438.

[38] C. Lu, L. Yang, B. Yan, L. Sun, P. Zhang, W. Zhang, Z. Sun, Nitrogen-doped Ti_3C_2 MXene: mechanism investigation and electrochemical analysis, *Adv. Funct. Mater.* 30 (2020), 2000852.

[39] H. Yang, Y. Zhou, Y. Wang, S. Hu, B. Wang, Q. Liao, H. Li, J. Bao, G. Ge, S. Jia, Three-dimensional flower-like phosphorus-doped $\text{g-C}_3\text{N}_4$ with a high surface area for visible-light photocatalytic hydrogen evolution, *J. Mater. Chem. A* 6 (2018) 16485–16494.

[40] H. Xu, J. Yi, X. She, Q. Liu, L. Song, S. Chen, Y. Yang, Y. Song, R. Vajtai, J. Lou, H. Li, S. Yuan, J. Wu, P.M. Ajayan, 2D heterostructure comprised of metallic 1T- MoS_2 /Monolayer O- $\text{g-C}_3\text{N}_4$ towards efficient photocatalytic hydrogen evolution, *Appl. Catal. B: Environ.* 220 (2018) 379–385.

[41] N. Tian, Y. Zhang, X. Li, K. Xiao, X. Du, F. Dong, G.I.N. Waterhouse, T. Zhang, H. Huang, Precursor-reforming protocol to 3D mesoporous $\text{g-C}_3\text{N}_4$ established by ultrathin self-doped nanosheets for superior hydrogen evolution, *Nano Energy* 38 (2017) 72–81.

[42] W.-J. Ong, L.-L. Tan, Y.H. Ng, S.-T. Yong, S.-P. Chai, Graphitic carbon nitride ($\text{g-C}_3\text{N}_4$)-based photocatalysts for artificial photosynthesis and environmental remediation: are we a step closer to achieving sustainability? *Chem. Rev.* 116 (2016) 7159–7329.

[43] Q. Liu, J. Shen, X. Yang, T. Zhang, H. Tang, 3D reduced graphene oxide aerogel-mediated Z-scheme photocatalytic system for highly efficient solar-driven water oxidation and removal of antibiotics, *Appl. Catal. B: Environ.* 232 (2018) 562–573.

[44] J. Liu, H. Xu, Y. Xu, Y. Song, J. Lian, Y. Zhao, L. Wang, L. Huang, H. Ji, H. Li, Graphene quantum dots modified mesoporous graphite carbon nitride with significant enhancement of photocatalytic activity, *Appl. Catal. B: Environ.* 207 (2017) 429–437.

[45] H. Wang, S. Jiang, W. Liu, X. Zhang, Q. Zhang, Y. Luo, Y. Xie, Ketones as molecular co-catalysts for boosting exciton-based photocatalytic molecular oxygen activation, *Angew. Chem., Int. Ed.* 59 (2020) 11093–11100.

[46] S. Luo, J. Ke, M. Yuan, Q. Zhang, P. Xie, L. Deng, S. Wang, CuInS_2 quantum dots embedded in Bi_2WO_6 nanoflowers for enhanced visible light photocatalytic removal of contaminants, *Appl. Catal. B: Environ.* 221 (2018) 215–222.

[47] X. Li, J. Hu, T. Yang, X. Yang, J. Qu, C.M. Li, Ultrafast Growth of High-Quality Monolayer WSe_2 on Au, *Nano Energy* 92 (2022), 106714.

[48] A. Meng, S. Wu, B. Cheng, J. Yu, J. Xu, Hierarchical $\text{TiO}_2/\text{Ni(OH)}_2$ composite fibers with enhanced photocatalytic CO_2 reduction performance, *J. Mater. Chem. A* 6 (2018) 4729–4736.

[49] X. Zhang, C. Yang, Z. Xue, C. Zhang, J. Qin, R. Liu, Spatial separation of charge carriers via heterogeneous structural defects in graphitic carbon nitride for photocatalytic hydrogen evolution, *ACS Appl. Nano Mater.* 3 (2020) 4428–4436.

[50] D. Zhao, C.-L. Dong, B. Wang, C. Chen, Y.-C. Huang, Z. Diao, S. Li, L. Guo, S. Shen, Synergy of dopants and defects in graphitic carbon nitride with exceptionally modulated band structures for efficient photocatalytic oxygen evolution, *Adv. Mater.* 31 (2019), 1903545.

[51] N. Tian, H. Huang, C. Liu, F. Dong, T. Zhang, X. Du, S. Yu, Y. Zhang, In situ co-pyrolysis fabrication of $\text{CeO}_2/\text{g-C}_3\text{N}_4$ n–n type heterojunction for synchronously promoting photo-induced oxidation and reduction properties, *J. Mater. Chem. A* 3 (2015) 17120–17129.

[52] Z. Lian, F. Wu, J. Zi, G. Li, W. Wang, H. Li, Infrared light-induced anomalous defect-mediated plasmonic hot electron transfer for enhanced photocatalytic hydrogen evolution, *J. Am. Chem. Soc.* 145 (2023) 15482–15487.

[53] S. Xiao, W. Dai, X. Liu, D. Pan, H. Zou, G. Li, G. Zhang, C. Su, D. Zhang, W. Chen, H. Li, Microwave-induced metal dissolution synthesis of core–shell copper nanowires/ ZnS for visible light photocatalytic H_2 evolution, *Adv. Energy Mater.* 9 (2019), 1900775.

[54] W. Wang, Y. Tao, J. Fan, Z. Yan, H. Shang, D.L. Phillips, M. Chen, G. Li, Fullerene–graphene acceptor drives ultrafast carrier dynamics for sustainable CdS photocatalytic hydrogen evolution, *Adv. Funct. Mater.* 32 (2022), 2201357.

[55] M.K. Bhunia, S. Melissen, M.R. Parida, P. Sarawade, J.-M. Basset, D.H. Anjum, O. F. Mohammed, P. Sautet, T. Le Bahers, K. Takanabe, Dendritic tip-on polytriazine-based carbon nitride photocatalyst with high hydrogen evolution activity, *Chem. Mater.* 27 (2015) 8237–8247.

[56] K.L. Corp, C.W. Schlenker, Ultrafast spectroscopy reveals electron-transfer cascade that improves hydrogen evolution with carbon nitride photocatalysts, *J. Am. Chem. Soc.* 139 (2017) 7904–7912.

[57] Z. Chen, Q. Zhang, Y. Luo, Experimental identification of ultrafast reverse hole transfer at the interface of the photoexcited methanol/graphitic carbon nitride system, *Angew. Chem., Int. Ed.* 57 (2018) 5320–5324.

[58] R. Godin, Y. Wang, M.A. Zwijnenburg, J. Tang, J.R. Durrant, Time-resolved spectroscopic investigation of charge trapping in carbon nitrides photocatalysts for hydrogen generation, *J. Am. Chem. Soc.* 139 (2017) 5216–5224.

[59] Q. Ruan, M.K. Bayazit, V. Kiran, J. Xie, Y. Wang, J. Tang, Key factors affecting photoelectrochemical performance of g-C₃N₄ polymer films, *Chem. Commun.* 55 (2019) 7191–7194.

[60] J. Fu, K. Liu, K. Jiang, H. Li, P. An, W. Li, N. Zhang, H. Li, X. Xu, H. Zhou, D. Tang, X. Wang, X. Qiu, M. Liu, Graphitic carbon nitride with dopant induced charge localization for enhanced photoreduction of CO₂ to CH₄, *Adv. Sci.* 6 (2019), 1900796.

[61] Y. Wang, P. Du, H. Pan, L. Fu, Y. Zhang, J. Chen, Y. Du, N. Tang, G. Liu, Increasing solar absorption of atomically thin 2D carbon nitride sheets for enhanced visible-light photocatalysis, *Adv. Mater.* 31 (2019), 1807540.